Research Article

A Computational Fluid dynamic (CFD) Modeling and FE Simulation of (NiBSi) Coating via Selective Laser Melting Process

Walaa Isam Rasool *, Ziad Aeyad Taha

Institute of Laser for Postgraduate Studies, University of Baghdad, Baghdad, Iraq
* Email address of the Corresponding Author:walaa.isam1101a@ilps.uobaghdad.edu.iq

Abstract: Powder bed methods, including selective laser melting (SLM), provide significant versatility in both design and manufacturing processes. However, the existing limitation of this method lies in its ability to produce single-material parts. For intricate multi-material requirements such as coating processes, optimal solutions involve a customized integration of diverse materials required to control the melting and solidification process within the different metals' interfaces. In this study, a computational fluid dynamic (CFD) model is created to analyze the two-metal SLM process, two types of metal used in this study NiBSi as a coat material on the surface of the stainless steel 316L. The model relies on classical physics laws to derive the governing equations, which are subsequently solved using the ANSYS FLUENT software. A User-Defined Function (UDF) written in C-language is utilized to define the heat source, and then it is executed over the cell face center in each time step. The melting of NiBSi powder on a stainless steel substrate was studied, and liquid mass fraction, laser power, and scanning speed were considered as the parameters of the investigation. The model undergoes a validation process using online-published data to confirm its accuracy and reliability before exploring four power values and four scanning speeds as parameters. The model predictions revealed a perfect interface region between the two metals and a clear correlation between the laser power and the size of the fully melted zone.

Keywords: CFD modeling, selective laser melting, two-metal SLM, coating.

1. Introduction

Additive manufacturing (AM) simplifies the production of complex components with customized geometric features, potentially heralding a new era in industrial evolution. Powder bed fusion (PBF) is considered as a principal and commonly used approach in metal AM processes [1-5]. Generally, it is categorized as electron powder bed fusion, selective laser sintering, direct metal laser sintering, and selective laser melting (SLM) [6-9]. Notably, among these, SLM represents a significant advancement in

AM technology, given its capability to produce components with a refined microstructure and exceptional mechanical properties [10-13]. During the SLM process, the temperature distribution undergoes rapid changes due to the energy beam's fast movement. Localized high energy input can result in a substantial temperature gradient, causing elevated residual stresses, and reduced wear resistance and hardness in the final products [14]. SLM parameters, including scanning speed, scanning strategy, spot size, and laser power exert considerable influence on the quality of the produced parts. Effectively optimizing these parameters is a crucial technique for attaining the targeted microstructure, densification, and mechanical properties of the produced parts [15, 16]. For instant various deficiencies, such as balling effects, or significant residual stresses can be managed by appropriately optimizing the scanning strategy in the AM process [17, 18]. Stainless steel is a frequently employed feed metal powder in the SLM process. This preference is attributed to various factors, including ease of use, safety, and relatively low cost. Specifically, 316L stainless steel finds extensive use in the aerospace industry due to its corrosion resistance and commendable specific strength [19]. However, Stainless steel components manufactured using SLM technology often exhibit low hardness and suboptimal surface quality. Hence, there is a genuine need for post-processing methods to improve protection and surface quality, as noted by Wang, Shen [20]. For example, the creation of a super-hydrophobic layer on the SLM substrate can significantly enhance corrosion resistance, self-cleaning properties, and resistance to snow accumulation. Techniques such as plasma etching, anodic oxidation, and phase separation are employed to develop the hydrophobic layer. However, it is acknowledged that these methods can be costly and involve harsh conditions, limiting their application. Alternatively, the SLM coating technique has recently emerged as having significant potential in selective deposition, allowing for the modulation of produced parts as needed [20]. In this regard, Konovalov, and Osintsev [21] investigated the feasibility of modifying the surface of the Ti-based alloy Ti-6.5Al-1Mo-1V-2Zr through the deposition of a SLM coating using Ni-based super alloy Ni-16Co-11Cr powder. The coating thickness varies between 70 and 130 μm, and the coating is composed of several phases, the main ones including titanium TiCo0.5Ni0.5, Ti0.25Al0.75, TiNi, TiCrAl. The nano hardness of the coating reaches a maximum of 10.5 GPa at a distance of 50 μm from the surface, which is twice as high as that of the Ti-based substrate. Another study by Shojaei and Trabia [22] examined the impact of applying a Ti/SiC Metal Matrix Nanocomposite coating (MMNC) to a Ti–6Al–4V substrate. The coating, deposited using the SLM technique, was tested alongside uncoated Ti–6Al–4V samples. Hypervelocity impact experiments, conducted with projectile velocities ranging from 3.7 to 5.4 km/s, revealed that the Ti/SiC MMNC coating improved impact resistance by reducing both impact diameter and crater depth. In a related study, Freitas, de Oliveira [23] applied boron-modified stainless steel coating to the surface of low carbon steel (AISI 1020) using SLM. The produced coatings, with thicknesses ranging from 200 to 600 μm, were metallurgically bonded to the substrate. This coating process exhibited wear resistance, displaying a specific wear rate of approximately 4.5×10^{-5} mm$^3 \cdot$N$^{-1} \cdot$m^{-1}, significantly outperforming the substrate with a specific wear rate of about 1.8×10^{-3} mm$^3 \cdot$N$^{-1} \cdot$m^{-1}. Cheng, Xu [24] used jet electrochemical machining to eliminate surface defects on SLM-formed parts prior to the application of a nickel coating, aimed at extending the operational service life. The electrochemical machining effectively eliminated nearly all surface defects from the SLM process, creating a consistent microporous structure that seamlessly integrated with the nickel coating. The resulting coating exhibited optimal corrosion resistance and binding strength. In a 3.5 wt% NaCl solution, the corrosion potential reached 20.196 V, with a maximum binding force of 35 N. Younsi, Boher [25] adopted the SLM to apply cobalt-based alloy coatings onto a C35 steel substrate.

The study explored the correlations among interlayer times, crystalline structures, iron dilution, and micro-hardness for varying numbers of layers. The findings showed that decreasing the interlayer time elevated the temperature within the melting bed and facilitated material transfer from the substrate. Also, the coating thickness comprised a Co-Cr-Fe mixture, delineated into two regions: a transition zone near the interface and a stabilized zone closer to the substrate. Notably, the actual coating thickness consistently increased when the interlayer time was reduced. Given that the SLM process comprises multiple parameters, time-consuming, and high costs, there is a demand for effective and precise numerical models to simulate the process [26]. Different numerical techniques have been presented recently to model the

process. In this context, Liu, and Fang proposed a mesoscale computational fluid dynamics (CFD) model to predict porosity in the SLM process [27]. The model takes into account the heat accumulation from previous tracks and the impact of scanning strategies for SS 316L and Ti-6Al-4V, respectively. Yu and Zhao developed an advanced three-dimensional computational model for precise simulations of the multiphysics multiphase processes associated with SLM. The model integrates a semi-coupled resolved CFD, multi-phase, and Discrete Element Method (DEM)[28] . A study by Xu, and Jiang [29] created a sophisticated 3D particle-scale CFD model for the selective parallel dual laser melting (SPDLM) process. The model enables the simulation of the dynamic behavior of molten pools of a Nickel-based superalloy. The study particularly focused on investigating phenomena such as necking, wetting, and pores near the overlapping region. The predicted results demonstrated that the SPDLM process enhances the re-melting rate and improves the wettability of the overlapping region. More recently, Anand and Chang [30] formulated a model to predict the properties of the melt pool on the first layer of the SLM process. A numerical simulation was conducted to acquire the transient temperature and velocity distribution throughout the process. Then, the obtained results were integrated with the proposed model. The model's efficacy was validated with experimental results and melt pool characteristics reported in previous publications. The model exhibited a Root Mean Square Error (RMSE) between 0.49 and 0.53. The review of existing literature indicates that numerous investigations have delved into improving the performance of the SLM process through diverse experimental and modeling techniques. However, a significant gap has been identified in the topic modeling of the SLM process, more particularly modeling coating using SLM.

In this study, an attempt has been made to construct a 3D model utilizing the CFD techniques to optimize the parameters of the NiBSi powder SLM coating process on an SS 316L substrate produced using another SLM process.

2. SLM coating background

Components manufactured by SLM technology are usually identified to exhibit insufficient hardness and subpar surface quality. Among the different technologies that have been tested to develop the quality of the produced parts' surface is the SLM. It has gained significant interest because of its versatility, adaptability, and numerous parameters that can be optimized. Laser energy, spot diameters, scanning speed, and hatch distance are some of these parameters. Conducting experimental optimization for such a broad range of parameters could be a time-consuming and costly operation. A well-established and verified numerical model can efficiently accomplish the task in a cost-effective and time-efficient manner, with a negligible margin of error.
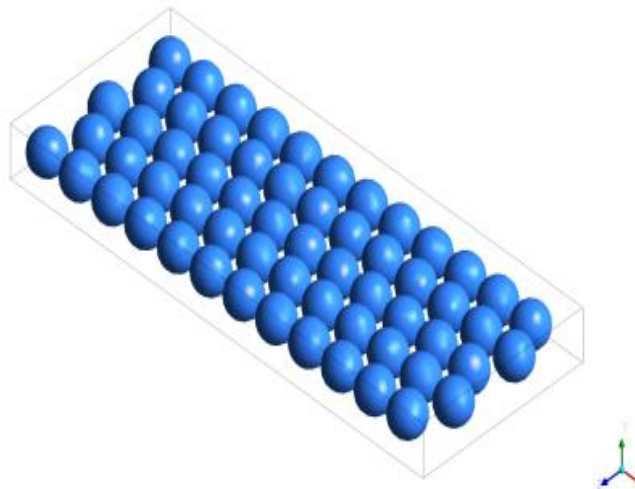

Fig.1: Geometry of the model showing the configuration and arrangement of the Ni powder particles.

The primary discretization technique employed in the CFD code is the finite volume method (FVM). In this approach, the governing equations for fluid dynamics are formulated using the conservation laws. It is noteworthy to mention that the CFD code allows for solving the fluid case either in a steady or unsteady manner using an iterative method. Initially, an approximate estimate is assumed, and then these values are iteratively adjusted until convergence is achieved. The term "convergence" in this context signifies that there will be no additional alteration in the variables during the subsequent iteration. ANSYS WORKPENCH R19.2 FLUENT software is used in this study to simulate the SLM process where a laser beam is considered as a heat source to melt the metal particles. The model considers the thermo-fluid parameters within the melting and solidification approach.

3. Governing equations

3.1 Continuity equation

The mass governing equation for the powder and solid domains takes the form as depicted in the provided Equation (1) which was given by Versteeg and Malalasekera [31].

$$\frac{\partial \rho}{\partial t} + \frac{\partial (\rho \boldsymbol{u})}{\partial x} + \frac{\partial (\rho \boldsymbol{v})}{\partial y} + \frac{\partial (\rho \boldsymbol{w})}{\partial z} \tag{1}$$

where ρ represents fluid density, t is time, and u denotes the velocity vectors for components u, v, and w in the x, y, and z directions, respectively. It is important to note that, in this particular case, the solution is based on a pressure-based solver with incompressible fluid, resulting in the density being equal to zero.

3.2 Navier–Stokes equation

This equation is crucial in the Computational Fluid Dynamics (CFD) code as it embodies the term of viscous stress in the balanced form of momentum. The following equation pertains to momentum in the x-direction, and similar formulations can be derived for the y- and z-directions [31]. It is evident from the equation below that there exists a connection between viscous stress and pressure within the fluid

$$\frac{\partial \rho u}{\partial t} + div\,(\rho uu) = -\frac{\partial p}{\partial x} + div\,(\mu\,grad\,u\,) + S_{Mx} \tag{2}$$

Equation (2) expresses the momentum in the *x*-direction, with p denoting pressure, μ representing fluid viscosity, and S stands for the source term. Typically, this equation is reformulated in a more general form, as indicated below [31]:

$$\rho u.\nabla u = -\nabla p + \nabla.\tau \tag{3}$$

here τ is the shear stress tensor and ∇ denotes $\frac{\partial}{\partial x} + \frac{\partial}{\partial y} + \frac{\partial}{\partial z}$

3.3 Energy equation

The energy equation is given by Versteeg and Malalasekera [31] as:

$$u\frac{\partial T}{\partial x} + v\frac{\partial T}{\partial y} = \alpha_{eff}\left(\frac{\partial^2 T}{\partial x^2} + \frac{\partial^2 T}{\partial y^2}\right) \tag{4}$$

The coefficient of average heat transfer (α) can be considered based on the total surface area.

3.4 Heat generation and distribution formulation

A volumetric heat source is suggested to play a role in facilitating the penetration of the laser beam into the powders [32]. The absorptivity profile group is employed in the model, presenting a volumetric Gaussian distribution that accounts for the penetration of the laser beam into the powder [33].

$$q = \frac{9PA}{R^2 \pi H \left(1 - \frac{1}{e^3}\right)} exp \left(\frac{-9(x^2 + y^2)}{R^2 \log\left(\frac{H}{z}\right)}\right) \tag{5}$$

Here P represents the laser power (W), R denotes the laser beam diameter (m), H indicates the heat source penetration depth (m), and A is the materials effective laser energy absorption, it is set as 0.8. ANSYS FLUENT software has limitations in certain cases that necessitate customization of functions or equations essential during simulation processes. Additionally, there are instances where calculations need to be performed based on specific equations at each time step or iterations over cell faces. FLUENT has limitations in this regard; therefore, a User Define Function (UDF) was employed. It is written in C-language, compiled, and interpreted during the simulation. Once interpreted, the function specified for defining the boundary condition, applying material properties, or setting the heat flux becomes available in the graphical interface of FLUENT [34]. In this study, the parameters of the laser have been incorporated into the User Define Function (UDF) and executed over the cell face center at each time step. The widely employed computational approach for comprehending the significance and impact of fluid turbulence behavior is through the use of turbulence models. Numerous turbulence models are integrated into CFD codes for solutions. It is established in the literature that the *k-ε* model delineates the interplay between two fundamental factors in fluid flow issues—kinetic energy and dissipation rate. This model is recognized for its efficacy in connecting the mechanistic effects of kinetic energy (k) and the dissipation rate (ε) of this energy [35].

4. Geometry formation and mesh creation

The model's geometric structure is formulated using WORKBENCH R19.1 and its design modeler software. This software facilitates the preparation of the model for subsequent stages, including meshing and solving. A two-dimensional CFD model is employed to simulate the interaction between the metal powder and the laser beam. The model, is configured with a transient option for a time-dependent solution, and it assumes an average diameter of 48 μm for the metal powder particles. The dimensions of the model are 450 μm in length, 200 μm in width, and 100 μm in thickness, as given in Fig. 2 below. Within the model, the particles are assumed to have a uniform spherical shape and have a uniform arrangement.
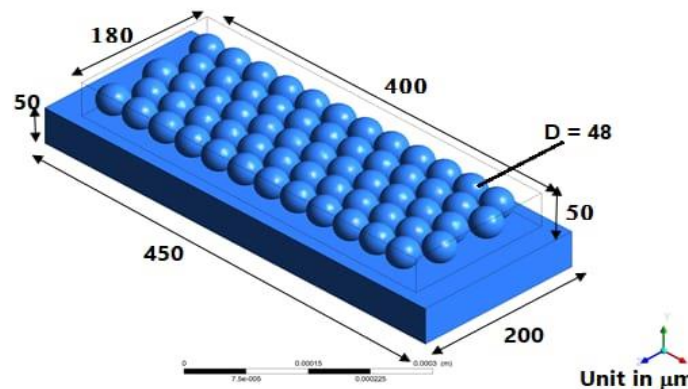

Fig. 2. The geometry of the model is utilized for the validation procedure and mesh analysis.

After establishing the model geometry, it is transferred to the meshing software, where four grids of mesh are created and then investigated in a comprehensive mesh study. The relevance auto mesh factor is configured with four values: 25, 50, 75, and 100. Fig.3 illustrates the mesh graph, where the average cell size is taken as 0.003 mm.
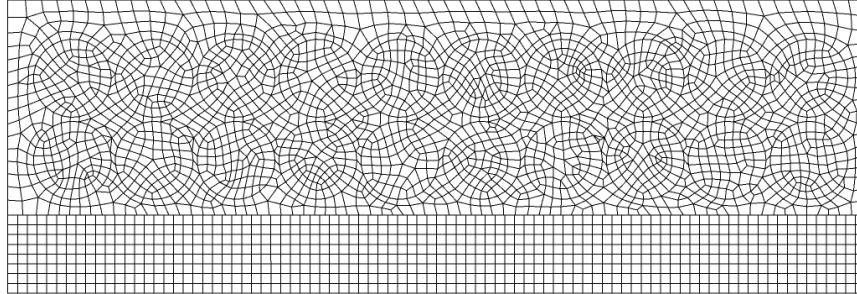

Fig.3. The configuration of the used mesh.

4.1 Mesh Independence Study

During the investigation of mesh independence, the generated grid cases were executed until the simulation data exhibited no divergence attributable to mesh-related issues. The maximum aspect ratio for the considered four mesh factors is less than 4. This value is deemed highly satisfactory and closely approximates the ideal value outlined in the ANSYS manual [36]. Tabel. 1 shows the mesh independence study data, revealing a notable distinction in mass fraction of 0.28 between grid No.1 and No.2, whereas the difference is only 0.01 for grid No.3 and No.4. Hence, grid No.3 was selected for all the cases in this study. It has approximately half the number of cells in comparison to grid No.4, leading to a substantial reduction in computational time.

Tabel. 1: The mesh independence study.

Grid No.	Total number of cells	Mass fraction
1	2300	0.93
2	3052	0.65
3	4624	0.36
4	10836	0.35

4.2 Solver setting

The solver settings comprise important factors including boundary conditions, solution methods, and convergence criteria. Initially, the solution needs to be determined whether the solution is in a steady or transient state. Following that, the gravity factor is selected, and an incompressible fluid flow option is chosen due to the constant density of the fluid. NiBSil material properties are specified, and the turbulence model employed is the K-ε model. Figure .4 illustrates the flowchart that is followed for preparing the computational model.
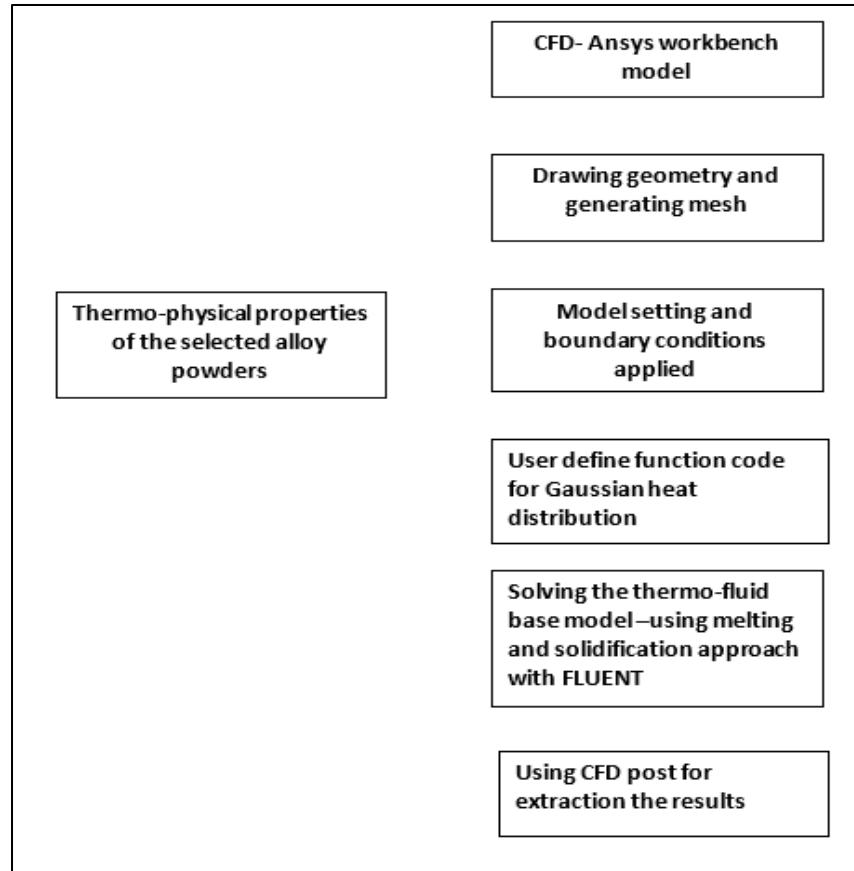
Fig. 4. Flowchart for ANSYS® simulation.

Boundary conditions play a crucial role as they define the physical model by specifying the characteristics of flow at the inlet and outlet, as well as determining whether parts are stationary or moving. In this simulation, all walls within the domain were designated as fixed with slip conditions. This implies that the fluid near the first cell that is adjacent to the wall possesses a velocity value equivalent to the main flow velocity. Regarding the solution method, the study opted for the Semi-Implicit Method for Pressure-Linked Equations (SIMPLE), employing pressure-velocity coupling algorithms. These algorithms are employed to calculate pressure based on the momentum and continuity equations sequentially. For each investigated case, the simulation is conducted using a time step size of 5e-06, encompassing a total of 30 time steps. Additionally, there are 20 iterations per time step, employing the assumed turbulent standard k-epsilon model. Monitoring the convergence is highly significant as it serves as a common practice to determine whether the solution aligns with the convergence criteria or not. Typically, the initial setting involves monitoring the residual values for momentum, continuity, and turbulence factors. Nonetheless, this method alone may not offer an accurate decision on solution convergence, as illustrated by the residual monitoring plot presented in

Fig. .
     In

Fig. the moment curve is employed for convergence monitoring, specifying the mass fraction as the convergence criteria in the designated region of interest, particularly within the initial layer of the NiBSi particles. A crucial step in any simulation involves assessing the convergence status for both transient and

steady-state solutions. Hence, in this study, solution convergence was evaluated in the region of interest. A point was established at a location of x=-0.955 and y= 0.055 mm, and the liquid fraction was continually monitored at this point until the variation in the liquid fraction was less than 1% per iteration. Figure 5 illustrates that after 250 iterations, no further changes occurred, providing a clear indication of solution convergence.
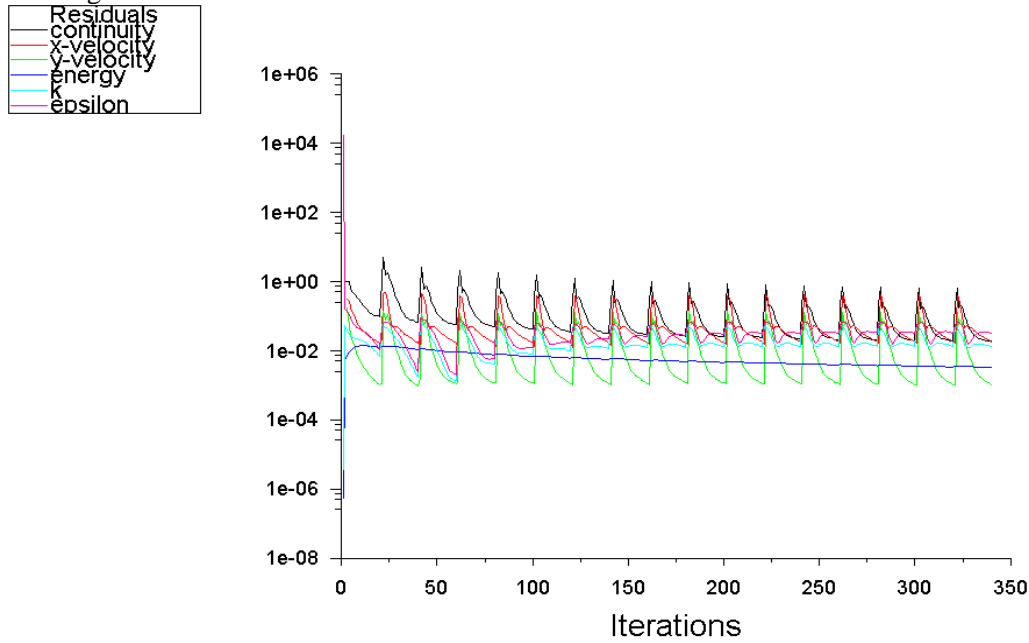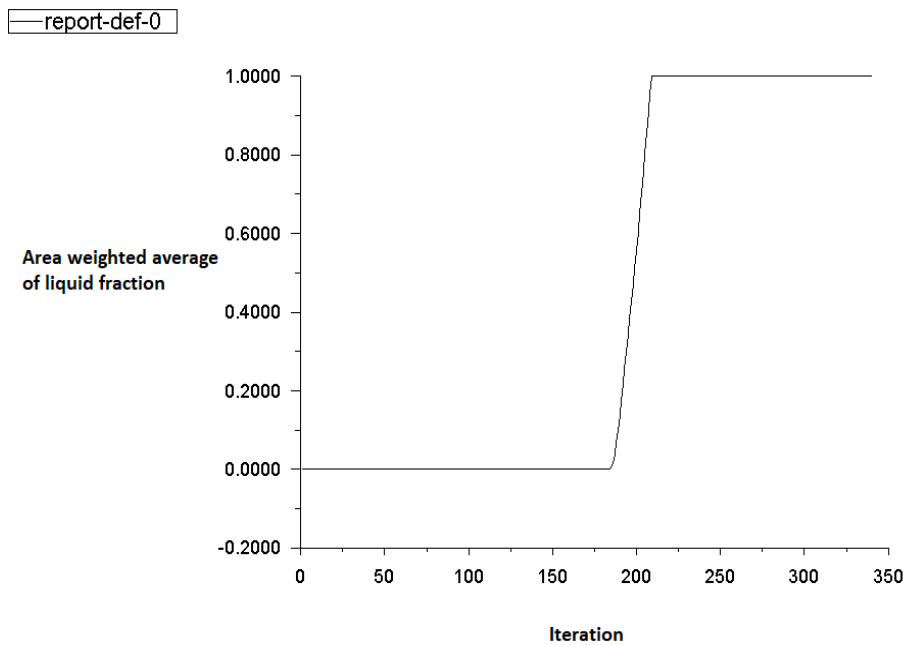
Fig. 5. Numerical solution residuals.

Fig. 5. Convergence graph for the liquid fraction value against iterations, specified at the point (x=-0.955 and y= 0.055 mm) within the domain.

4.3 Model validation

The validation process is a crucial task for any model to confirm and ensure the reliability of the results. In this study, the validation of the model is done by replicating the investigation results of a study conducted by Xia, Gu [37] where Inconel 718 Ni, a nickel-based superalloy, is utilized. Tabel. 2 provides detailed physical properties of the used powder in addition to some of the implemented SLM process parameters.

Tabel. 2: The material properties and parameters utilized in the SLM process [37].

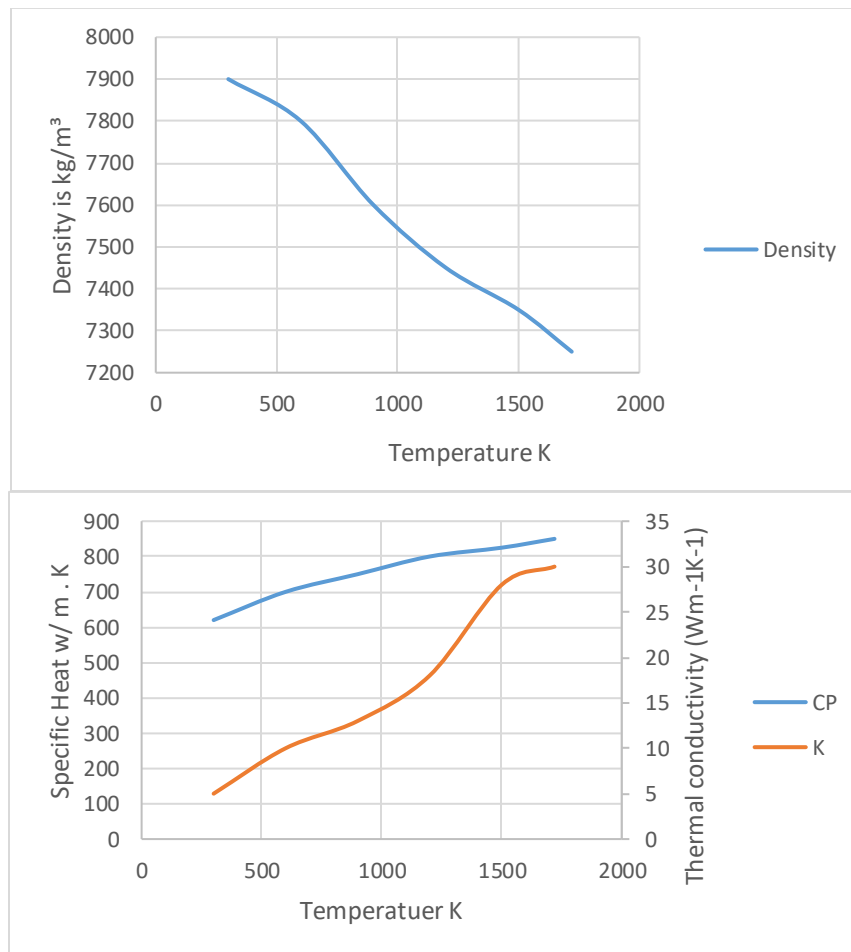| Properties	Value
Density, ρ (Kg/m^3)	8200
Absorption of superalloy powder, A	0.8
Ambient temperature, T_o (K)	293
Powder layer thickness, d (μm)	50
Radius of the laser beam, D (μm)	35
Hatch spacing, s (μm)	50
Laser power, P (W)	77.5, 88.6, 99.8, 110
Scanning speed, v (mm/s)	400

Fig.7. The properties of stainless steel 316L as a function of temperature.

In order to validate the current model a comparison was conducted with the work of Xia, Gu [37] and using the material's properties and process parameters listed in Tabel. 1. The iso-surface method was employed to predict the depth of the molten pool for temperature and mass fraction variables. The average value of three positions was assessed using a CFD probe. The iso-surface threshold for mass fraction was established at 0.9, indicating that regions below this value represent solids, while those above signify liquids. A similar approach was employed for the iso-surface temperature, utilizing a threshold of 1600K, as depicted in
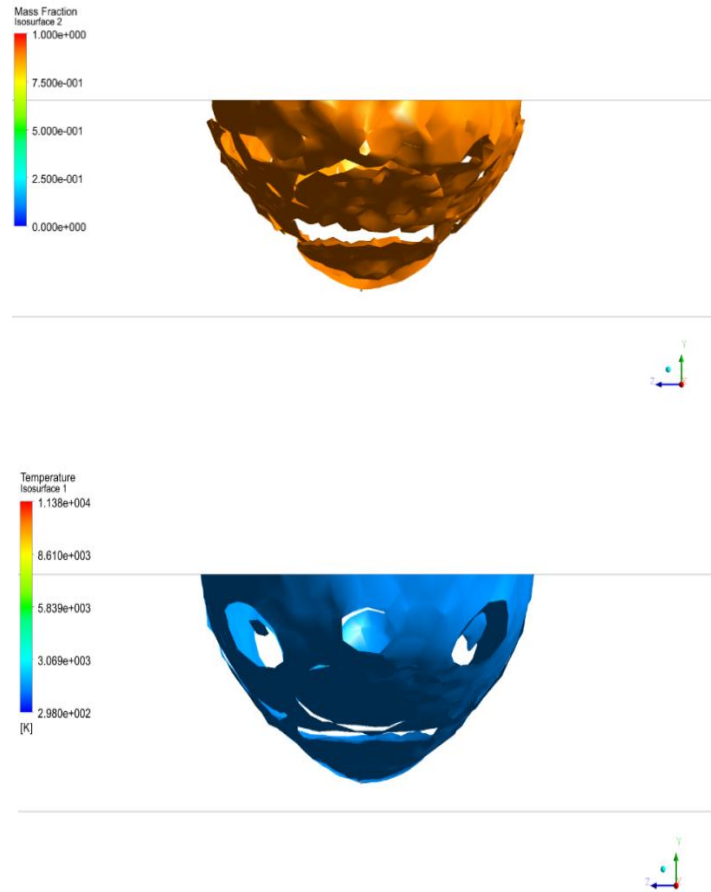
Fig.

Fig. 8. Iso surface plot; (a) mass fraction assuming 0.9 is liquids phase, (b) iso temperature surface at below solidus temperature.

Tabel.3 A comparison between the model-predicated results and data given in Xia, Gu [37].

Laser power (watt)	Temperature (K)			Weld pool depth (µm)		
	Model prediction	Xia, Gu [37]	Differences (%)	Model prediction	Xia, Gu [37]	Differences (%)
77.5	2080	1905	9.19	25.9	28.3	8.48
88.6	2136	2178	1.93	27.09	26.5	2.23
99.8	2180	2308	5.55	29	25.8	12.40
110	2207	2539	13.08	26.6	23.6	12.71

3. Predicted results

In order to determine the mass faction of the liquid phase in the molten pool a virtual line (a-a) is created at the center of the domain in the middle section. The length of the line is 200 micrometers, and it is located just below the interface between NiBSi powder and stainless steel layer at a 6 micrometer in the negative y direction, as shown in the

Fig.. At this line, the validated mass fraction in the molten pool is computed. Additionally, its position serves as a reference for establishing all parameters in the following sections.
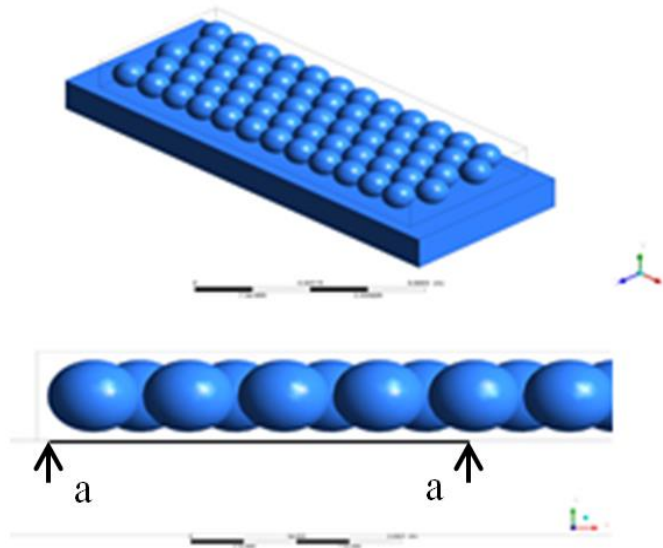

Fig.9: The 3D model shows the orientation of the proposed line a-a where the predicted mass fraction profile and other process parameters are calculated.

Tabel. **4** outlines the design of the undertaken parametric investigation, involving variations in laser power (40, 45, 50, and 55 Watts), and adjustments in scanning speed (60, 65, 70, and 74 mm/s), while maintaining a constant laser spot diameter of 15 µm. The table also illustrates the impact of varying scanning speeds, corresponding to each of the power intensities, on both the liquid fraction area and the average pool thickness. The results affirm a minimal impact of the examined parameters on the liquid fraction area, with the scanning speed demonstrating negligible effects on the average pool thickness. However, the laser power exhibits a notable influence on the average pool thickness. Results in Fig. demonstrate the correlations between temperature and both laser power and scanning speed. It is observed that these relationships are directly proportional and inversely proportional, respectively.

Fig. 4 illustrates the distribution of mass fractions along lines a-a exemplified in

Fig.. Fig. 4 (a to d) shows the mass fraction profile corresponding to various operation parameters, including laser power and scanning speed, as outlined in Tabel. 4. In all the figures (a to c), the attainment of a mass fraction value of one is evident, affirming the successful achievement of complete melting. However, the location along line a-a where complete melting occurs is observed to be contingent on both laser power and scanning speed. In general, the full melting onset point along line a-a appears to be influenced by the scanning speed for a particular laser power value. As the speed increases, the onset point shifts in the positive x-direction, and vice versa. On the other hand, the impact of laser power appears different; an increase in power serves to broaden the region where full melting occurs for all considered scanning speeds.

Tabel. 4: cases considered for the simulation with different input power and laser scan speed with a constant laser spot size.

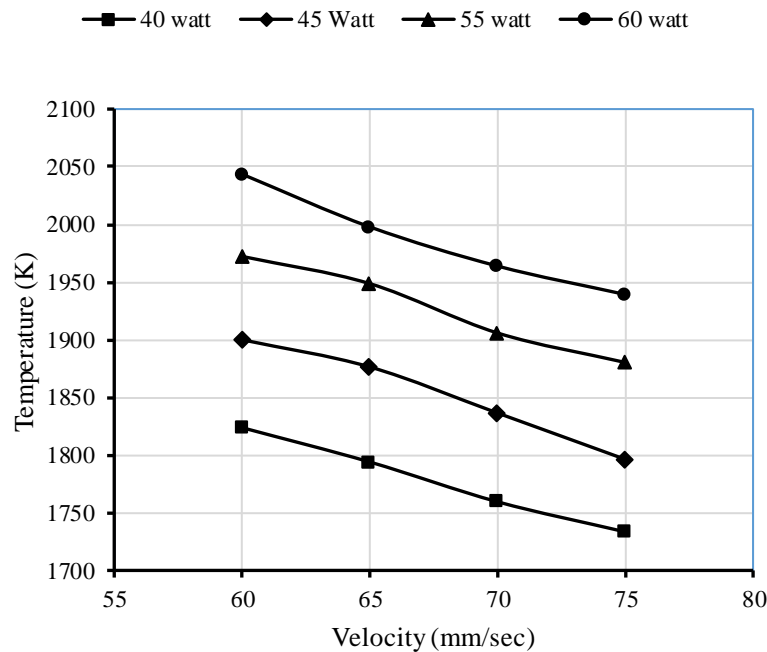| No.	Power (Watt)	Scan speed (mm/s)	Liquid fraction area on Isosurface 1 ([mm²])	Average pool thickness (µm)
1	40	60	0.0235	65.01
2	40	65	0.0234	65.1
3	40	70	0.029	65
4	40	75	0.0238	65
5	45	60	0.0259	69.2
6	45	65	0.02506	69.45
7	45	70	0.0249	69.5
8	45	75	0.0254	69.6
9	50	60	0.0284	69.6
10	50	65	0.027	71
11	50	70	0.0269	70.1
12	50	75	0.0251	69
13	55	60	0.0308	74.4
14	55	65	0.0302	74.7
15	55	70	0.0299	74.5
16	55	75	0.02978	74.5

Fig.10: The relationship between the temperature and scanning speed at different laser powers.
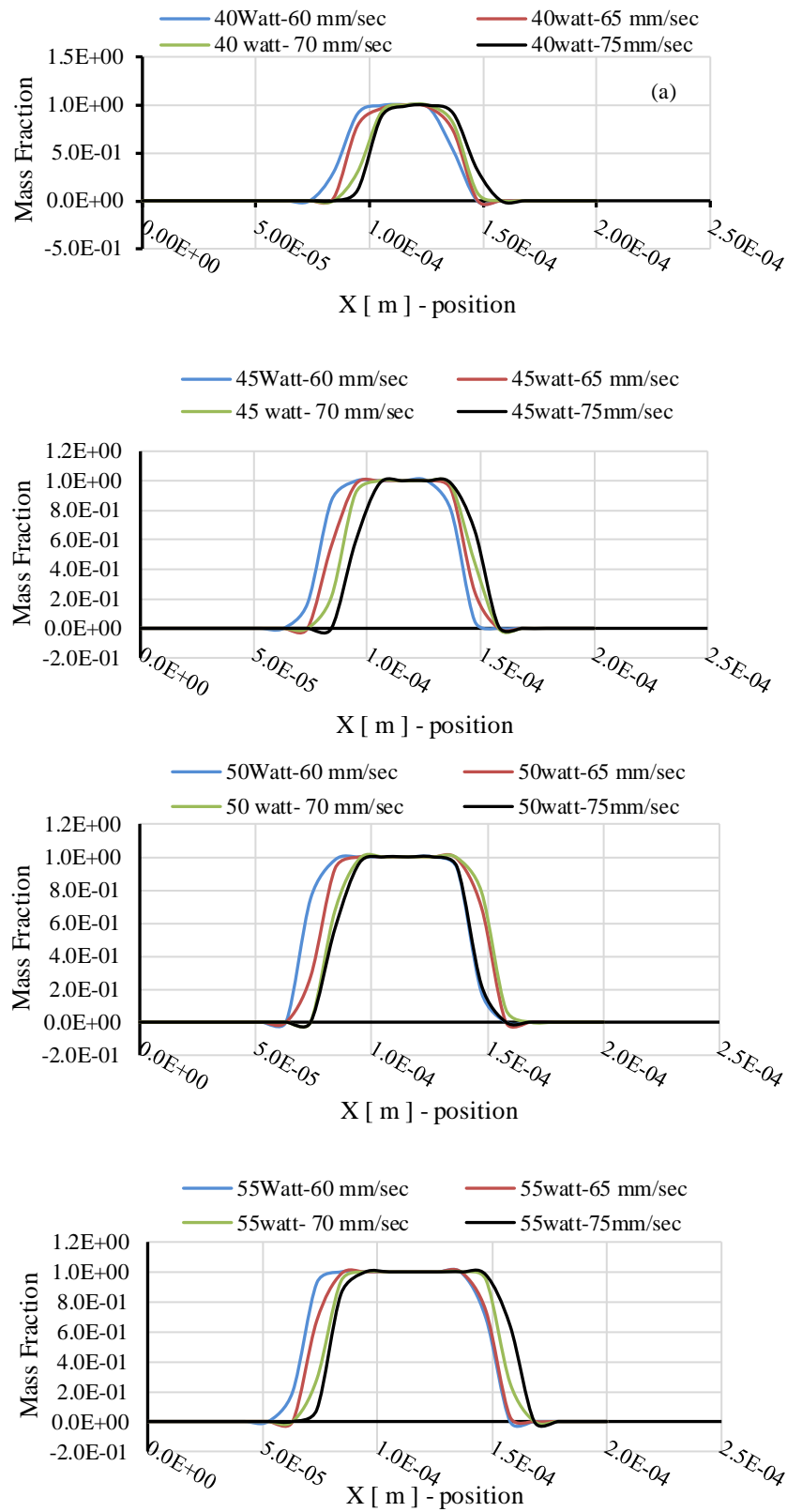
Fig. 4: Mass fraction profile along lines a-a.

In Fig.5, mass fraction contours and iso-surfaces are displayed in a 3D layout, with a value of 0.9 indicating a fully liquid state. Subfigures a, b, c, and d depict instances where the scanning speed is maintained at 65 mm/s, while the laser power is varied at 40, 45, 50, and 55 Watts, respectively. An observable proportional relationship exists between laser power and the size of the fully melted interface region that occurs between the NiBSi particle and the stainless steel substrate.
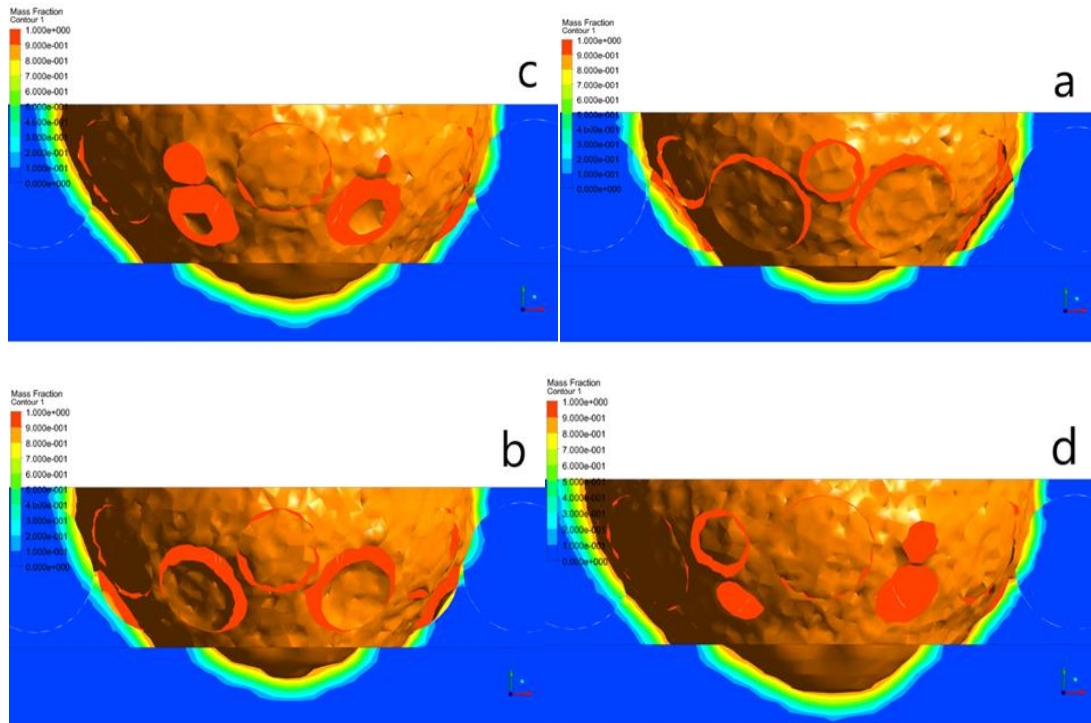

Fig.5: Liquid phase mass fraction contour and iso surface obtained using 65 mm/sec scanning speed, and laser power of (a) 40 Watt, (b) 45 Watt, (c) 50 Watt, and (d) 55 Watt.

5. Conclusions

A CFD model is presented in this study to simulate and analyze two-metal SLM processes typically associated with specific applications like coating. Such applications demand a tailored integration of two metals, necessitating control over the melting and solidification processes at the interface of different metals. The model utilized fundamental principles of classical physics to establish the governing equations, which are then resolved through the application of ANSYS FLUENT software. Moreover, a UDF function was written in C-language to define the heat source. Our study novelty can be explained in the coming points.

1- The model validation was demonstrated by considering the melting of NiBSi powder on a stainless steel substrate, utilizing experimental data available online.

2- The study was carried out to examine process parameters such as liquid mass fraction, laser power, and scanning speed. Four power values and four scanning speeds were used in the study.

3- This consideration will give a real distribution of temperature during coating process.

4- The model predictions exhibited significant concordance with the experimental results (87-98%), validating the model's reliability. Moreover, the parametric study showed a strong correlation between laser power and the size of the fully melted zone. It also affirmed the existence of an optimal interface region between the two metals.

References

[1] Robinson, J., et al., Determination of the effect of scan strategy on residual stress in laser powder bed fusion additive manufacturing. Additive manufacturing, 2018. 23: p. 13-24.

[2] Al-Aloosi, R.A., et al., Influence of scanning velocity on a CoCrMoW alloy built via selective laser melting: microstructure, mechanical, and tribological properties. Journal of Materials Engineering and Performance, 2023. 32(15): p. 6717-6724.

[3] Al-Aloosi,R.A., et al., Efect of scan speed on corrosion and tribocorrosion prperties of coblet-chroium alloy in situe produced by selective laser melting. Rapid prototyping Journal, 2023.

[4] AKM, Yousef., et al., Building a simulation model for the prediction of temperature distribution in pulsed laser spot welding of dissimilar low carbon steel 1020 to aluminum alloy 6061. AIP Conference Proceedings, 2011. 1315(1): p.1425-1430.

[5] MS, Hassan., et al., Synthesis and modeling of temperature distribution for nanoscales produced using Nd:YAG laser. Journal of Nanotechnology, 2016.

[6] Fina, F., S. Gaisford, and A.W. Basit, Powder bed fusion: The working process, current applications and opportunities. 3D printing of pharmaceuticals, 2018: p. 81-105.

[7] Hadi, R.M. and Z.A. Taha, Effect of SiC Addition on Microhardness and Relative Density during Selective Laser Melting of 316L Stainless Steel. Journal of Engineering, 2022. 2022.

[8] Hadi, R. and Z.A. Taha, Mechanical Properties of AISI 316L Stainless Steel Produced Via Selective Laser Melting. Iraqi Journal of Laser, 2022. 21(1): p. 51-60.

[9] Hadi, R.M. and Z.A. Taha, Selective laser melting of Inconel 601 alloy using nanosecond fibre laser. Periodicals of Engineering and Natural Sciences, 2022. 10(3): p. 161-171.

[10] Li, C., et al., On the simulation scalability of predicting residual stress and distortion in selective laser melting. Journal of Manufacturing Science and Engineering, 2018. 140(4): p. 041013.

[11] ZA, Taha., et al., M athematical modeling of laser-assisted transmission lap welding of polymers. Scripta Materialia, 2009. 60(8): p. 663-666.

[12] MM,Hanon., et al., Experimental and theoretical investigation of the drilling of alumina ceramic using Nd:YAG pulsed laser. Optics and Lser Technology, 2012. 44(4): p. 913-922.

[13] HA, Jasim., et al., Process development and monitoring in stripping of a highly transparent polymeric paint with ns- pulsed fiber laser. Optics and Laser Technology, 2017. 39: p. 60-66.

[14] He, K. and X. Zhao, 3D Thermal Finite Element Analysis of the SLM 316L Parts with Microstructural Correlations. Complexity, 2018.

[15] Xiong, W., et al., Effect of selective laser melting parameters on morphology, microstructure, densification and mechanical properties of supersaturated silver alloy. Materials & Design, 2019. 170: p. 107697.

[16] Lo, Y.-L., B.-Y. Liu, and H.-C. Tran, Optimized hatch space selection in double-scanning track selective laser melting process. The International Journal of Advanced Manufacturing Technology, 2019. 105: p. 2989-3006.

[17] Zhang, X., et al., Microstructure evolution during selective laser melting of metallic materials: A review. Journal of Laser Applications, 2019. 31(3).

[18] Mugwagwa, L., et al., Evaluation of the impact of scanning strategies on residual stresses in selective laser melting. The International Journal of Advanced Manufacturing Technology, 2019. 102: p. 2441-2450.

[19] Kong, D., et al., Mechanical properties and corrosion behavior of selective laser melted 316L stainless steel after different heat treatment processes. Journal of Materials Science & Technology, 2019. 35(7): p. 1499-1507.

[20] Wang, Z., et al., Superhydrophobic nickel coatings fabricated by scanning electrodeposition on stainless steel formed by selective laser melting. Surface and Coatings Technology, 2019. 377: p. 124886.

[21] Konovalov, S., et al., Surface modification of Ti-based alloy by selective laser melting of Ni-based superalloy powder. Journal of Materials Research and Technology, 2020. 9(4): p. 8796-8807.

[22] Shojaei, P., et al., Enhancing hypervelocity impact resistance of titanium substrate using Ti/SiC Metal Matrix Nanocomposite coating. Composites Part B: Engineering, 2020. 194: p. 108068.

[23] Freitas, B.J.M., et al., Microstructural characterization and wear resistance of boride-reinforced steel coatings produced by Selective Laser Melting (SLM). Surface and Coatings Technology, 2021. 426: p. 127779.

[24] Cheng, H., et al., High-performance nickel coating on SLM 316L stainless steel processed by jet electrochemical machining and jet electrodeposition. Proceedings of the Institution of Mechanical Engineers, Part B: Journal of Engineering Manufacture, 2022. 236(4): p. 462-472.

[25] Younsi, T., C. Boher, and A. Soveja, Influence of interlayer time on the microstructural state of CoCrMo coatings applied by selective laser melting on an iron-based substrate for different numbers of layers. Materials Today Communications, 2022. 32: p. 103776.

[26] Zhou, R., H. Liu, and H. Wang, Modeling and simulation of metal selective laser melting process: a critical review. The International Journal of Advanced Manufacturing Technology, 2022. 121(9-10): p. 5693-5706.

[27] Liu, B., et al., Predicting the porosity defects in selective laser melting (SLM) by molten pool geometry. International Journal of Mechanical Sciences, 2022. 228: p. 107478.

[28] Yu, T. and J. Zhao, Quantitative simulation of selective laser melting of metals enabled by new high-fidelity multiphase, multiphysics computational tool. Computer Methods in Applied Mechanics and Engineering, 2022. 399: p. 115422.

[29] Xu, G.-G., et al., Particle-scale computational fluid dynamics simulation on selective parallel dual-laser melting of nickel-based superalloy. Journal of Manufacturing Processes, 2022. 73: p. 197-206.

[30] Anand, N., et al., Development of a Comprehensive Model for Predicting Melt Pool Characteristics with Dissimilar Materials in Selective Laser Melting Processes. Journal of Materials Processing Technology, 2023: p. 118069.

[31] Versteeg, H.K. and W. Malalasekera, An introduction to computational fluid dynamics: the finite volume method. 2007: Pearson education.

[32] Kik, T., Heat source models in numerical simulations of laser welding. Materials, 2020. 13(11): p. 2653.

[33] Zhang, Z., et al., 3-Dimensional heat transfer modeling for laser powder-bed fusion additive manufacturing with volumetric heat sources based on varied thermal conductivity and absorptivity. Optics & Laser Technology, 2019. 109: p. 297-312.

[34] Hasan, A., CFD modelling of friction stir welding (FSW) process of AZ31 magnesium alloy using volume of fluid method. Journal of Materials Research and Technology, 2019. 8(2): p. 1819-1827.

[35] Dellinger, G., et al., Computational fluid dynamics modeling for the design of Archimedes Screw Generator. Renewable energy, 2018. 118: p. 847-857.

[36] Ansys, I., ANSYS meshing user's guide. vol, 2013. 15317: p. 724-746.

[37] Xia, M., et al., Selective laser melting 3D printing of Ni-based superalloy: understanding thermodynamic mechanisms. Science Bulletin, 2016. 61(13): p. 1013-1022.

العناصر المحددة لطلاء من النيكل -بورون -سيليكون المنتج بواسطة الصهر بالليزر الانتقائي

ولاء عصام رسول ، زياد اياد طه

معهد الليزر للدراسات العليا، جامعة بغداد، بغداد، العراق

*البريد الالكتروني للباحث: walaa.isam1101a@ilps.uobaghdad.edu.iq

الخلاصة: يتم استخدام نموذج ديناميكية الموائع المحوسبة في هذه الدراسة لمحاكاة وتحليل عمليات الصهر بالليزر الانتقائي ثنائية المعدن المرتبطة عادةً بتطبيقات محددة مثل الطلاء. تتطلب مثل هذه التطبيقات تكاملًا مخصصًا لمعدنين، مما يستلزم التحكم في عمليات الذوبان والتصلب عند السطح البيني للمعادن المختلفة. تم استخدام المبادئ للفيزياء الكلاسيكية لإنشاء المعادلات الحاكمة، والتي يتم حلها بعد ذلك من خلال تطبيق برنامج ANSYS FLUENT. علاوة على ذلك، تمت كتابة وظيفة محدده من قبل المستخدم UDF بلغة Cسي لتحديد مصدر الحرارة. تم إثبات التحقق من صحة النموذج من خلال النظر في ذوبان مسحوق NiBSi على ركيزة من الفولاذ المقاوم للصدأ، وذلك باستخدام البيانات التجريبية المتاحة عبر الإنترنت. بعد ذلك، تم إجراء دراسة لفحص معلمات العملية مثل جزء الكتلة السائلة، وقوة الليزر، وسرعة المسح. تم استخدام أربع قيم طاقة وأربع سرعات مسح في الدراسة. أظهرت تنبؤات النموذج توافقًا كبيرًا مع النتائج التجريبية (87-98%)، مما يؤكد موثوقية النموذج. علاوة على ذلك، أظهرت الدراسة البارامترية وجود علاقة قوية بين قوة الليزر وحجم المنطقة المنصهرة بالكامل. كما أكدت وجود منطقة واجهة مثالية بين المعدنين.